Journal of Nuclear Materials 518 (2019) 177–189

Contents lists available at ScienceDirect

Journal of Nuclear Materials

journal homepage: www.elsevier.com/locate/jnucmat

Direct measurement of hydrogen diffusivity and solubility limits in Zircaloy 2 (formula unit of $ZrH_{0.0155}$) using incoherent quasi-elastic neutron scattering

Brent J. Heuser [a, *], Timothy R. Prisk [b], Jun-li Lin [a], Tanya J. Dax [b], Yongfeng Zhang [c]

[a] Department of Nuclear, Plasma, and Radiological Engineering, University of Illinois, Urbana, IL, 61801, USA
[b] Center for Neutron Research National Institute of Standards and Technology, Gaithersburg, MD, 20899-6100, USA
[c] Fuels Modeling and Simulations, Idaho National Laboratory, Idaho Falls, ID, 83415, USA

ARTICLE INFO

Article history:
Received 22 September 2018
Received in revised form
15 February 2019
Accepted 25 February 2019
Available online 8 March 2019

Keywords:
Hydrogen diffusion
Neutron scattering
Activation energy
Zircaloy
Solubility limit

ABSTRACT

The diffusivity of hydrogen is an important property of light water nuclear reactor (LWR) fuel cladding. LWR cladding absorbs hydrogen during normal operation, a contributing factor to embrittlement that decreases the lifetime of the fuel. Mass transport of hydrogen is dictated by an Arrhenius behavior typical of solid state diffusion and the associated activation energy is therefore a property relevant to LWR fuel performance. We have used incoherent quasi-elastic neutron scattering (QENS) to directly measure the diffusivity of hydrogen in recrystallized Zircaloy 2 with a hydrogen concentration of 170 μg/g. We rely upon the low-Q expansion for long-range diffusion to determine diffusivity as a function of temperature between 572 and 780 K. We find the diffusivity is given by $D(T) = 0.0067 \exp(-0.461\ eV/kT)$ [cm^2/s] below 670 K and by $D(T) = 0.0012 \exp(-0.36\ eV/kT)$ [cm^2/s] above 670 K. Our activation energy below 670 K agrees with the value typically used to assess hydrogen diffusivity in LWR cladding [Kearns, Journal of Nuclear Materials 43 (1972) 330], but is approximately 20% lower above 670 K. The two different activation barriers are attributed to impurity trapping of hydrogen solutes at lower temperature that ceases to influence diffusivity at higher temperature. The application of the Oriani model for diffusion with impurity trapping to our system demonstrates the plausibility of this hypothesis. We believe this mechanism may be responsible for historical discrepancies of measured hydrogen diffusivity in Zr-based alloys. The elastic intensity versus temperature in fixed window scans exhibit inflection points that are in good agreement with the published terminal solid solution solubility limits for hydrogen in Zircaloy 2.

1. Introduction

Zirconium-based alloys are used for light water nuclear reactor (LWR) fuel cladding throughout the world. This cladding undergoes uniform corrosion during normal operation that results in formation of a water-side oxide layer and hydrogen pickup. Radiolysis enhances cladding corrosion. The cladding also experiences significant fast neutron displacement cascade damage. Fuel swelling and fission gas release at intermediate to high burnup lead to large tensile stresses within the cladding. All of these factors act to limit the lifetime of LWR fuel.

The mass transport and phase behavior of hydrogen in Zr-based alloys is an important component to LWR fuel performance modeling and to the overall response of the cladding to the LWR environment. Hydrogen diffusivity and solid solution solubility are included in the BISON thermomechanical finite element analysis code [1,2]. The diffusivity of hydrogen implemented in BISON by Courty et al. and Davis *et al.* [1,2] is the often cited [[1–7] for example] measurements of Kearns [8]. Other experimental values of hydrogen diffusivity in unalloyed Zr exist [[8,9] and reference therein]. All known experimental data on hydrogen diffusivity in Zr and Zr alloys date to the 1950s, 1960s, and 1970s, employed diffusion couples or a hydride surface layer and typically hot vacuum extraction for hydrogen concentration analysis. The Kearns work is often cited because it was the most extensive, including pure zirconium, Zircaloy 2, Zircaloy 4, the effect of heat treatment, and the effect of sample orientation of rolled plate and swaged material. The influence of composition (pure Zr versus Zircaloy 2 and 4),

* Corresponding author.
E-mail address: bheuser@illinois.edu (B.J. Heuser).

https://doi.org/10.1016/j.jnucmat.2019.02.045
0022-3115/

orientation (transverse, longitudinal, and normal directions), cold work, and grain size on hydrogen diffusivity are all deemed small based on the work of Kearns.

Hydrogen diffuses in the HCP α–Zr lattice by translation jumps between neighboring tetragonal (T) interstitial sites. These sites are connected along the c-axis direction and have an activation barrier much lower than tetrahedral to octahedral (O) or O-O jumps [9–12]. The T-T jump distance in α–Zr is $2 \cdot \frac{c}{8}[0001] = 1.29$ Å. Recent advanced computations have been performed to quantify hydrogen diffusion in Zr and Zr alloys [9,10,12,13]. Christensen *et al.* found an activation energy ($E_a = 0.434$ eV) similar to the experimental value of Kearns ($E_a = 0.462$ eV). The diffusion constant was found to be significantly lower (0.0013 [cm^2/s] versus 0.007 [cm^2/s]), leading to lower calculated diffusivities compared to measured values. A ballistic effect involving multiple jumps not captured in the computational approach is a possible explanation of the discrepancy [9]. Zhang *et al.* have recently investigated the effect of the hydrogen solute-impurity binding enthalpy on diffusivity in Zircaloy and find that lower diffusivity is associated with impurity trapping [13].

The temperature-dependent solid solution phase behavior of hydrogen in Zr-based alloys is another important property because axial and azimuthal temperature variations exist in a LWR core, as do radial temperature gradients within the clad wall. The effect of the latter leads to the so-called hydride rim structure [14,15] in LWR cladding that results in circumferential hydride platelet formation in the colder water-side region [16,17]. The solid solution phase behavior is given by the terminal solid solution solubility curve for dissolution (TSSd) and precipitation (TSSp) of the hydride phase. The two curves, together defining the temperature hysteresis, are known from solubility measurements [18–25]. Significant variations exist between these measurements. We discuss these variations within the context of our solubility limit determination in subsequent sections.

Neutron scattering techniques are ideally suited to study hydrogen in metals [26–29]. This is because the neutron-nuclear interaction does not vary systematically with atomic number and because thermal neutrons have energies similar to lattice vibrational modes in solids. The application of incoherent quasi-elastic neutron scattering (QENS) to study hydrogen diffusivity is an excellent example of the utility of neutron scattering, with measurements dating to the late 1960s and 1970s [30–32] and continuing to present day [26,33,34]. The effectiveness of QENS to quantify diffusivity in crystalline solids rests with sensitivity to diffusive motions on the micro-eV energy scale. This energy range is well separated from the milli-eV scale associated with phonon modes. The current generation of backscattering QENS spectrometers, such as the High Flux Backscattering Spectrometer (HFBS) [35] used here, have optimized resolution of order 10^0 μeV and are sensitive to broadening of the elastic peak of order 10^{-1} μeV [28]. The sensitivity of QENS is enhanced for hydrogen because of the large incoherent scattering cross section (80.26 b). Another advantage of QENS for the H-Zr system is the significantly lower hydrogen diffusivity in the δ-Zr hydride phase over the temperature range studied here [36]. This has the effect of collapsing QENS intensity from hydrogen diffusion in the *hydride phase* into the instrumental resolution. The peak broadening of the QENS measurement for our system then is due solely to the faster diffusive motion of solid solution hydrogen regardless of the phase fraction of δ-hydride. On the other hand, the QENS intensity is determined by the fraction of diffusing hydrogen and is therefore a sensitive measure of the phase transformation during heating and cooling; in other words, the TSS behavior.

We present QENS measurements of Zircaloy 2 at a hydrogen concentration of 170 parts per million by mass (μg/g) hydrogen (formula unit of $ZrH_{0.0155}$) as a function of temperature between 572 and 780 K using the HFBS at the NIST Center for Neutron Research. Analysis allows us to determine the Arrhenius behavior of hydrogen self-diffusion (that is, diffusion in the absence of a concentration gradient) over this temperature range. The self-diffusion coefficient and the chemical diffusion coefficient (diffusion with a concentration gradient) are equivalent in the dilute solution conditions used here. We compare our results to the currently accepted diffusion constant and activation energy of Kearns and find notable differences above 670 K. Finally, our analysis has unique sensitive to the TSS behavior and we find good agreement with accepted solubility limits.

2. Materials and methods

2.1. As-received Zircaloy 2 recrystallization

Beta-quenched, un-recrystallized rolled Zircaloy 2 plate was supplied by ATI Specialty Materials with a composition consistent with UNS R60802 specification [37]. The as-received plate was 3.4 mm thick. Forty (40) bars with a 4×3.4 mm^2 cross section and 45 mm long were cut from the plate using electric discharge machining to avoid plastic deformation associated with mechanical cutting. All surfaces were mechanically abraded with 1200 grit paper to remove surface contamination. Two sets of bars were cut; one set of 20 bars with the long axis corresponding to the rolling direction (RD) of the as-received plate, the other set corresponding to the transverse direction (TD). This resulted in a sample orientation average over the normal direction (ND), the RD, and the TD during QENS analysis. In addition, the HFBS analyzer crystal array accepts significant vertical angular divergence (the nominal Q plane is horizontal) and this results in additional averaging for our sample material. We therefore consider our diffusivity measurements to be an effective orientation average.

The *in situ* QENS temperature cycling employed here involved temperatures in excess of 750 K that would induce recrystallization. The sample material was therefore annealed in flowing Ar gas at 973 K for six (6) hours to ensure complete recrystallization prior to the QENS measurements. The research purity (99.999% source gas) Ar gas stream was purified by a getter furnace upstream of the anneal furnace. The bars were separated on all four sides using stainless steel wire for this annealing procedure and for the hydrogen loading. Basal plane pole figures of our sample material before and after the annealing procedure are shown in Fig. 1. The effect of annealing is to induce a change in texture consistent with recrystallization of rolled plate [17,38–40]. The total mass of the sample for QENS analysis was 149.50 g and the total hydrogen inventory based on the measured concentration from the gas phase loading procedure was approximately 26 mg. Composition analysis of the post-annealed, post-hydrogen loaded material performed by NSL Analytical is shown in Table 1.

2.2. Hydrogen loading

Hydrogen loading to a concentration of 170 μg/g (formula unit of $ZrH_{0.0155}$) was performed using a Sievert's apparatus described previously [41] by exposure of the sample material to H_2 gas at 673 K. Briefly, this system allows controlled exposure of materials (Zircaloy 2 in the present case) to hydrogen gas in a constant volume with accurate absolute pressure measurement in a stainless steel gas manifold. The measured pressure decreases as the specimen absorbs solute atoms. The ideal gas law can then be used to calculate the absorbed solute concentration once equilibrium is obtained for a given sample mass and the measured total pressure reduction. The hydrogen loading process we employed sequentially

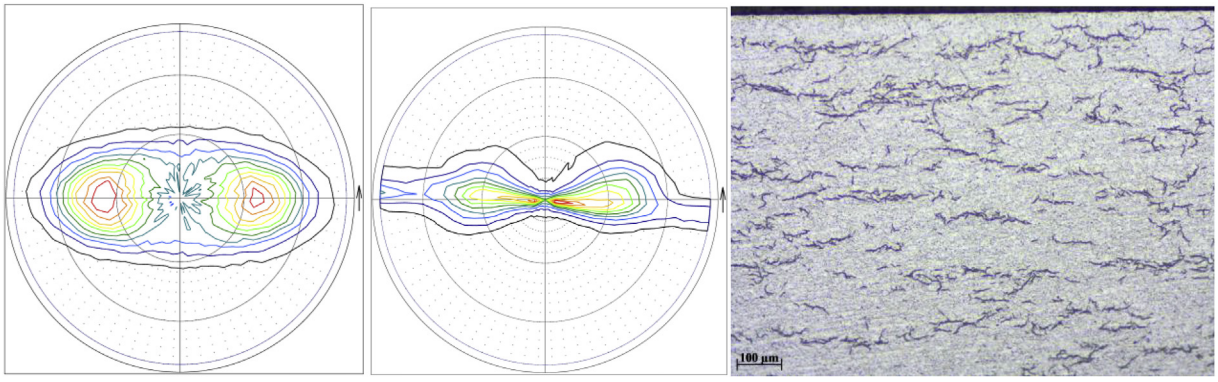

Fig. 1. Basal plane pole figure of the as-received (left) and fully recrystallized (middle) Zy2 sample material used in this study. The TD is horizontal, the RD vertical, and the ND orthogonal to the plane of the paper for the two pole figures. Annealing induces stronger texture oriented toward the ND, similar to that expected for recrystallized Zy2 plate [36]. The texture for the as-received rolled plate is consistent with a lack of a final recrystallization step used for cold rolled Zy2 [17] and looks similar to stress-relieved Zy4 texture [39,40]. The right-hand optical micrograph shows the hydride morphology in the ND-TD plane after hydrogen loading and thermal cycling. The free surface exposed to hydrogen gas is shown at the top of the micrograph. The hydride platelets are uniformly distributed thought out the bulk of the Zy2 material.

Table 1
Chemical composition of post-recrystallization, post-hydrogen loaded Zy2 sample material used in this study. Composition data are from a 5 g assay for metal elements and a 0.1 g assay for hydrogen and oxygen. Uncertainty in concentrations quoted from NSL Analytical.

Material	Sn [mass %]	Fe [mass %]	Cr [mass %]	Ni [mass %]	O [mass %]	H [mass %]	Zr [mass %]
Zircaloy 2	1.44 (0.14)	0.086 (0.013)	0.057 (0.009)	0.034 (0.005)	0.12 (0.02)	0.015 (0.002)	98.2 (0.1)

exposed the heated sample to a hydrogen gas pressures of 1200 Pa followed by 8266 Pa. The first 1200-Pa exposure was performed to monitor the absorption kinetics and terminated at a final H_2 pressure of 800 Pa. The kinetics of gas absorption was slow at this temperature even though the sample material had a large surface area (~260 cm^2). The second 8266-Pa exposure was allowed to proceed to equilibrium. Gas pressure was monitored with four capacitance manometers spanning a pressure range from 10^5 Pa to 10^{-2} Pa. Absorption to equilibrium for the second exposure (8266 Pa → 15 Pa) required 12 h. The total H_2 pressure change was 8666 Pa, corresponding to a hydrogen concentration of 170 μg/g calculated using the ideal gas law, the known volume of the Sievert's system (4.549 l), and the total sample mass (187 g, with some bars set aside and not used for QENS analysis). This concentration is within the uncertainty from the NSL chemical analysis (150(20) μg/g in Table 1). We estimate the error in our concentration value to be less than 5% and therefore use 170 μg/g for the hydrogen concentration throughout this manuscript.

The sample material then underwent two thermal cycles, heating to a temperature well above the TSSd (approximately 650 K at 170 μg/g [22]) under equilibrium H_2 gas pressure. The purpose of the thermal cycles was to place all hydrogen in solid solution and allow sufficient time for the elimination of possible concentration gradients via diffusion. The first cycle involved heating to 880 K at a heating rate of 1 K/min immediately after H_2 gas pressure equilibrium was achieved at 673 K and holding for 12 h. The sample material was then cooled to 423 K at a rate of 1 K/min. The second thermal cycle was to heat the sample from 423 K to 780 K at a rate of 1 K/min, hold for 2 h, and then cool to room temperature at a rate of 1 K/min. Metallographic analysis was performed to characterize the hydride phase morphology after these two thermal cycles. The result of this analysis is shown in Fig. 1, an optical micrograph of the sample plane orthogonal to the rolling direction (the ND-TD plane). The hydride particles are distributed uniformly though out this plane, demonstrating that any hydrogen concentration gradients that may have existed after loading were eliminated by thermal cycling.

2.3. Temperature mockup experiments

Two sample cans were used for the QENS measurements on the HFBS. Table 2 lists all neutron scattering measurements performed for this work. An unsealed Al sample can was used for measurements at 653 K and lower, while a sealed Ti can filled with 1.3×10^5 Pa of He exchange gas was used at 670 K and higher. Both cans had an inner diameter of 29 mm. Two exceptions to these temperature ranges for the respective cans were a 710 K Al can measurement and a 295 K Ti can measurement. The motivation for using the sealed Ti can with the He exchange gas was to minimize temperature gradients along the length of the Zy2 bars at higher temperature.

Ex situ temperature mockup experiments to measure the temperature gradients are described below. The unsealed Al sample can was under vacuum common to the bottom loading closed-cycle refrigerator (CCR) vacuum. The presence of the He exchange gas in the sealed Ti can had no effect on the QENS response of our samples, but did reduce the temperature gradient along the length of the sample slightly (~2 K). Two heat/thermal shields were used to reduce temperature gradients along the length of the sample. The sample can, heat shields, and mounted thermocouples were placed within the CCR vacuum can. In addition, waded Al foil was inserted between the upper lid (which was connected to the CCR heater) and the top of the Zy2 bars to promote heat transport. Two thermocouples (TCs) were used to record temperature, the control sensor at the heating stage and the second mounted to the top of the sample can.

Three mockup experiments were performed with the same CCR and Zy2 sample after QENS analysis to quantify the temperature gradient during a fixed window scan (FWS described in the next section) transient (Al can only) and steady state QENS measurement protocols (Al and Ti cans). The temperature transient mockup was identical to the fixed window scan described below: 300 K → 750 K → 300 K at a ramp rate of 0.5 K/min (Al can). The steady state mockup was followed the QENS measurement temperature trajectory (Al can): ramping to the specified temperature

Table 2
List of FWS and QENS measurement parameters, hydrogen diffusivity at each temperature point.

QENS/FWS	Can Top Temperature [K][a]	Corrected Sample Temperature [K][c]	Dynamic Range [μeV]	Time [h]	D [x10^{-6} cm^2/s]
FWS	300 → 750	NA	NA	15	NA
FWS	750 → 400	NA	NA	11.7	NA
QENS[b]	780↑	771	±36	9	4.9 ± 0.2
QENS[b]	765↑	757	±36	8	4.54 ± 0.21
QENS[b]	750↑	743	±36	8	3.82 ± 0.12
QENS[b]	730↑	723	±36	17	3.41 ± 0.07
QENS	710↑	703	±15	4	2.98 ± 0.09
QENS[b]	690↑	686	±15	9	2.62 ± 0.08
QENS[b]	670↑	666	±15	8	2.05 ± 0.06
QENS[b]	670↑	666	±36	8	2.08 ± 0.04
QENS	670↑	664	±15	8	2.14 ± 0.07
QENS	653↑	648	±15	8	1.70 ± 0.04
QENS	653↓	648	±15	8	1.68 ± 0.04
QENS	630↑	626	±36	8	1.28 ± 0.02
QENS	613↑	609	±15	8	0.96 ± 0.01
QENS	613↑	609	±15	8	0.98 ± 0.02
QENS	613↓	609	±15	5	1.05 ± 0.03
QENS	613↓	609	±15	8	1.02 ± 0.02
QENS	583↑	580	±15	8	0.62 ± 0.02
QENS	583↓	580	±15	8	0.72 ± 0.01
QENS	572↑	569	±15	8	0.55 ± 0.02
QENS	572↓	569	±15	8	0.59 ± 0.01
QENS	295↓	NA	±15	3	resolution
QENS[b]	295	NA	±36	7	resolution
QENS vanadium	295	NA	±15	21	resolution

[a] Up and down arrows indicate can-top steady state temperature reached during heating or cooling, respectively. Heating and cooling rates of 0.5 °C/min for FWS or 1.5 °C/min plus a 30 min hold for steady state QENS.
[b] QENS measured using sealed Ti can with He exchange gas. All other QENS measurements performed with an unsealed Al can under vacuum.
[c] Corrected sample temperature defined as the can-top temperature minus ½ ∇T.

point at 1.5 K/min and holding for 90 min, with all temperature points measured upon heating and cooling to 750 K. A similar protocol was used for the Ti can. Three TCs were used, the first placed at the top of the heater stage (the control sensor), second at the top of the sample can, and the third at the bottom of the sample can. All three TCs were sheathed with Al to avoid thermal shorting. In addition, the drop down or can-bottom TC was insulated with a fiberglass sheath along the length from just above the heater stage to just above the can bottom. This was done to eliminate heat transport along the Al sheath, an effect that would lead to smaller recorded temperature gradients along the length of the sample. We define the temperature gradient as the can-top TC minus the can-bottom TC reading. A cross calibration measurement of the two TCs at the QENS temperature points was also performed. The can-top and can-bottom TCs were mounted side-by-side to the heater stage to record the common temperature.

The cross calibration measurement demonstrated that the can bottom TC consistently recorded a 2-K lower temperature relative to the can-top TC above ambient temperature, leading to a larger apparent temperature gradient, denoted here as ∇T. We subtract this difference from the steady state mockup temperature gradient measurement. The temperature gradients were nearly identical for the unsealed Al can and the sealed Ti can with He exchange gas, but with the latter slightly smaller (~2 K).

The measured gradients between the can-top and can-bottom for the Al can were as follows: ∇T = 6.5 K (572 K and 583 K↑); ∇T = 8 K (613 K↑); ∇T = 9 K (630 K↑); ∇T = 10 K (653 K↑); ∇T = 13.5 K (710 K↑); ∇T = 7 K (630 K↓); ∇T = 2.5 K (550 K↓). The measured gradients between the can-top and can-bottom for the Ti can were as follows: ∇T = 8 K (670 K↑); T = 9 K (690 K↑); ∇T = 14 K (730 K↑); ∇T = 14 K (750 K↑); ∇T = 16 K (765 K↑); ∇T = 18 K (780 K↓). Here T↓ and T↑ denote steady state temperature upon cooling and heating, respectively, and all temperature points were reached with a 1.5 K/min ramp rate. Equilibrium with respect to steady state temperature at the bottom of the can and therefore with respect to the temperature gradient required approximately 30 min at all temperatures upon heating and cooling. Slightly lower gradients were observed upon cooling; 7 K versus 9 K at 630 K for the Al can for example.

Our QENS measurement procedure employed at 30 min hold prior to data acquisition. QENS intensity was recorded in 30 min time bins and we also examined these individually to confirm steady state with respect to line broadening. We create an Arrhenius plot of diffusivities in the Results Section. The temperatures used for this plot are average or corrected sample temperature: can top temperature minus ½∇T at each temperature point. The corrected temperatures are listed in Table 2. The error bars in the independent variable (x = 1000/T, where T is average sample temperature) are given by $\sigma_x = \left(1000/T^2\right)\sigma_T$, where we simply use one half of the measured gradient as the standard deviation, $\sigma_T = ½\nabla T$.

The temperature gradient during the 300 K→750 K→300 K FWS transient using the Al can with a ramp rate of 0.5 K/min was measured in the third mock up experiment. The magnitude of the gradients were smaller than those above due to the slower ramp rates. For example, upon heating between 400 and 650 K the gradients increased in an approximately linear manner from 5 K to 10 K, overall 2 K–3 K lower than the steady state mock up experiment. Gradients less than 5 K were observed below 700 K during cooling in the FWS mock up experiment. We observe two inflection points in the FWS data presented below, one on the heating curve and the other on the cooling curve. These inflection points correspond to the solubility limits of hydrogen in Zy2 and occur at approximately 650 K (heating) and 575 K (cooling). We therefore are most concerned with the temperature gradients along the sample in the vicinity of these inflections. The gradients are approximately 10 K and 0 K for heating and cooling, respectively. The latter effectively zero gradient is a consequence of heat removal from the top of the can and the can-top minus can-bottom difference becoming less than zero below approximately 570 K. The fact

that the gradient was close to zero upon cooling as the system crossed the TSSp was fortuitous and had a positive impact on identification of this solubility limit.

2.4. Neutron scattering experimental procedure

The High-Flux Backscattering Spectrometer (HFBS) employs a velocity selector, a phase space transformation chopper, a Doppler drive monochromator, and single crystal Si wafer focusing analyzer array to minimize the energy resolution of the elastic peak in backscattering geometry [35]. The phase space transformation chopper boosts the measured QENS intensity by transforming incident wavevector spread to larger angular divergence, thereby taking greater advantage of the focusing analyzer crystal array [35]. The instrument operates at a neutron wavelength of $\lambda = 6.271$ Å. This wavelength satisfies the Bragg condition for the (111) reflection of Si near 90°. An array of sixteen (16) ^{3}He filled detectors record the neutron intensity over a wavevector transfer (Q) range of 0.25 $Å^{-1}$ to 1.75 $Å^{-1}$. We note that this detector array has been updated since the publication of Reference 35 to extend the measured Q range to lower values. The HFBS can operate in two modes, one in which the Doppler drive is in motion at a frequency set by the user that determines the dynamic range of the QENS measurement and the second in which the Doppler drive is stationary and only the elastic intensity is recorded [35]. The second mode of operation is referred to as a fixed window scan (FWS) and is a useful way to determine the onset of QENS versus temperature.

We performed four sets of QENS measurements on the HFBS over a two-year period. All involved *in situ* temperature cycles. The same sample material was also used for a neutron Compton scattering experiment (to be published elsewhere) between the first and second QENS runs and this involved a temperature cycle as well. Equilibrium with respect to temperature at each measurement point was ensured i) by using a slow heating and cooling rates (0.5 K/min or 1.5 K/min) with generally small (10 K–20 K) temperature transients and long (8 h in most cases) QENS measurements at steady state, ii) holding at temperature for 30 min prior to data acquisition, and iii) confirming that the QENS intensity was invariant and therefore the sample temperature was at steady state. We also confirmed *ex situ* that hydrogen does not outgas from Zy2 at 780 K under vacuum prior to the first QENS measurement. All HFBS measurements are listed in Table 2. The up and down arrows in Table 2 indicate if the steady-state temperature was reached upon heating or cooling, respectively. This information is relevant for our consideration of the temperature hysteresis. The first neutron scattering experiment we performed, a fixed window scan that did not collect QENS intensity, involved *in situ* heating from ambient temperature to 750 K followed by cooling to 400 K at a rate of 0.5°/min. This represents an additional thermal cycle with the sample material held above the TSSd for approximately 5 h.

Quasi-elastic neutron scattering analysis requires a measurement of the instrument resolution. The resolution can be dependent on the sample size and composition. Therefore, the most accurate measurement of instrumental resolution is with the sample in place and all motions frozen. In our case, this is accomplished by the 295-K QENS measurements since the diffusivity of hydrogen (which is in the δ-hydride phase) at ambient temperature is sufficiently slow so that the QENS intensity within the elastic peak. We demonstrate this below. A set of temperatures (572 K, 583 K, 613 K, and 653 K) were repeated upon heating and cooling. This was done to investigate the effect of the temperature hysteresis. The QENS *intensity* was dependent on this effect. As expected, however, no effect was observed for *diffusivity* (determined from the QENS peak width) at common temperatures upon heating or cooling and this establishes reproducibility.

Two dynamic ranges were used, ±15 μeV and ±36 μeV, with the higher range used at higher sample temperature. This was done to capture greater QENS broadening due to faster diffusion at higher temperature since the QENS peak width scales with the diffusivity and diffusivity increases exponentially with temperature. An instrumental resolution was required for each dynamic range and this was accomplished by measuring the sample at ambient temperature (295 K, see Table 2). We also make use of an instrumental resolution measurement using vanadium (a pure incoherent scatterer) at ambient temperature at ±15 μeV to confirm the lack of QENS intensity from our sample material at ambient temperature.

3. Theory

The intensity measured in a QENS experiment is proportional to the dynamic structure factor, $S(Q,\omega)$, which is related to the double differential neutron scattering cross section via,

$$\frac{d^2\sigma}{d\Omega d\omega} = \frac{k}{k_o}\left[\frac{\sigma_{coh}}{4\pi}S_{coh}(\mathbf{Q},\ \omega) + \frac{\sigma_{inc}}{4\pi}S_{inc}(\mathbf{Q},\ \omega)\right] \tag{1}$$

where k_o and k are the incident and scattered wavevector, respectively, S_{coh} $(\mathbf{Q},\omega)$ and S_{inc} $(\mathbf{Q},\omega)$ are the coherent and incoherent dynamic structure factors, respectively, and σ_{coh} and σ_{inc} are the respective neutron scattering cross sections. The two forms of S $(\mathbf{Q},\omega)$ contain correlations between the same nucleus at different times (incoherent scattering) and correlations between different nuclei at different times (interference effects associated with coherent scattering, both elastic and inelastic). The data fitting used here assumes the zero-phonon incoherent dynamic structure factor is given by,

$$S_{inc}(\mathbf{Q},\omega) = e^{-2W}\left(A_0(\mathbf{Q})\delta(\omega) + \sum_{j=1}^{n} A_j(\mathbf{Q})L_j(\mathbf{Q},\omega)\right) \otimes R(\mathbf{Q},\omega) + B(\mathbf{Q},\omega) \tag{2}$$

where the product $A_o\delta(\omega)$ is the time-independent elastic contribution (dominated by elastic scattering from Zr atoms), the products A_jL_j are the quasi-elastic contributions, and B (Q,ω) is the background. The delta function in the elastic term is a consequence of the Fourier time transform integral associated with the intermediate scattering function for nuclei at fixed positions in space (that is, with frozen motions). The elastic and quasi-elastic intensity contributions are convoluted with the instrument resolution function R (Q,ω) and attenuated by the Debye-Waller factor e^{-2W}. Data analysis accounts for the instrumental resolution by mathematically convoluting a measurement of a representative sample (here we have only one sample) at low temperature (so that all hydrogen diffusive motion is frozen) with a delta function.

We are concerned with diffusive motion of hydrogen solutes in a crystal lattice; incoherent quasi-elastic scattering. The quasi-elastic contribution to the dynamic structure factor for long-range diffusion is given by a single Lorentzian function [31],

$$L(\mathbf{Q},\ \omega) = \frac{1}{\pi}\frac{f(\mathbf{Q})}{f(\mathbf{Q})^2 + \omega^2}, \tag{3}$$

where $f(\mathbf{Q})$ is the Lorentzian half-width. The orientation-average width $f(Q)$ for diffusion with discrete jump distance l is given by Ref. [32],

$$\hbar f(Q) = \hbar\omega_L = E_L = \frac{\hbar}{\tau}\left(1 - \frac{sin(Ql)}{Ql}\right) \cong \frac{\hbar}{\tau}\left[\frac{(Ql)^2}{6} - \frac{(Ql)^4}{120} + O(Ql)^6\right] \cong \hbar DQ^2, \quad (4)$$

where the Taylor expansion about $Ql = 0$ is shown and we use the Einstein equation for three-dimensional random motion $D = l^2/(6\tau)$ to write E_L in final form. We refer to this as the low-Q expansion result, a form that can be obtained directly from Fick's second law without invoking a discrete jump model [31]. We only keep the quadratic term for E_L since our data quality, which is good considering the low hydrogen inventory, does not support a 4th order correction. We determine the temperature dependent diffusivity using the low-Q expansion result to create an Arrhenius plot in the next section. We do not use the jump diffusion model because the Q range of the HFBS, which is typical of backscattering spectrometers, does not extend to sufficiently high values to capture the first peak in the sin $(Ql)/(Ql)$ term for $l = 1.29$ Å, the T-T jump distance in Zr. This is discussed in the next section.

4. Results

An example of the line broadening associated with QENS from hydrogen diffusion in our Zy2 sample material at 614 K (T↓, ±15 μeV dynamic range) is shown in Fig. 2. Data fitting used the Data, Analysis, and Visualization Environment (DAVE) software package [42]. The fit includes the convolution of the 295 K measurement with a delta function and a Lorentzian. A linear background term was included in the fit but is not shown. The primary source of background intensity is inelastic phonon scattering which is flat on the μeV energy scale. Significant broadening is evident due to QENS from the diffusion of hydrogen. The 295 K resolution measurement in Fig. 2, on the other hand, exhibits no QENS intensity. The fit in Fig. 2 only includes the resolution measurement (using vanadium) convoluted with a delta function and demonstrates this measurement is a valid quantification of instrumental resolution. The lack QENS at 295 K in Fig. 3 is consistent with the very low solid solution solubility of hydrogen in Zircaloy (or Zr in general) at ambient temperature and the significantly lower diffusivity of hydrogen in the δ hydride phase [36].

Diffusivity at each temperature point is determined by fitting the low-Q QENS data to Equation (4). This is shown in Fig. 4 for selected temperatures. The diffusivities for all temperature points from the best fit of Equation (4) are listed in Table 2. Fig. 4 inset is an example of a best fit to the isotropic diffusion model of Chudley and Elliot [32]. Although a maxima is observed in this data set that is

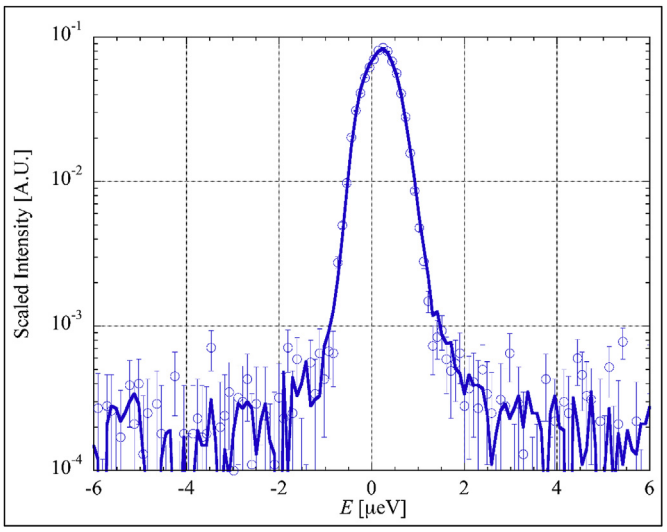

Fig. 3. QENS measurement at 295 K (T↓, ±15 μeV dynamic range, Q = 0.747 Å^{-1}, group 6) and fitting. Fitting only includes the instrumental resolution (vanadium at ambient temperature) convolution with a delta function and a linear background term (not shown). The lack of QENS broadening is clear when these data are compared to those in Fig. 2. The large statistical fluctuations in the fitted curve beyond the elastic peak are due to the propagation of noise in the vanadium measurement in the numerical convolution fitting procedure.

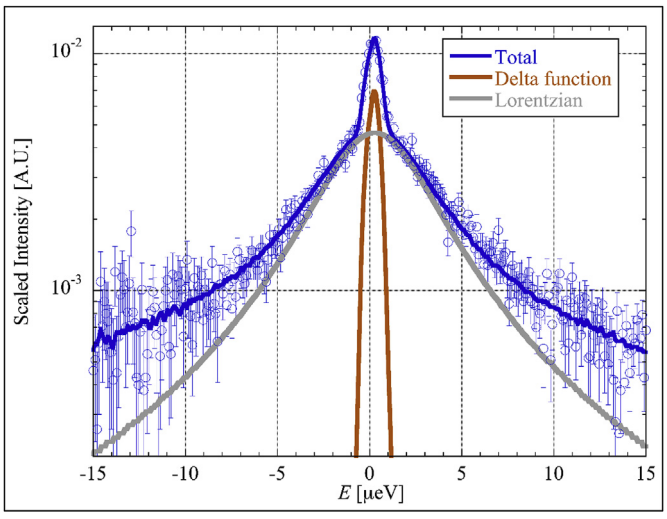

Fig. 2. QENS measurement at 613 K (T↓, ±15 μeV dynamic range, Q = 0.747 Å^{-1}, group 6) and fitting. Significant QENS intensity is observed that induces line broadening beyond the instrumental resolution. The QENS intensity is fit with a single Lorentzian and a delta function convoluted with the 295 K sample resolution measurement. A linear background term was included in the fitting but is not shown. Error bars throughout all figures represent one standard deviation.

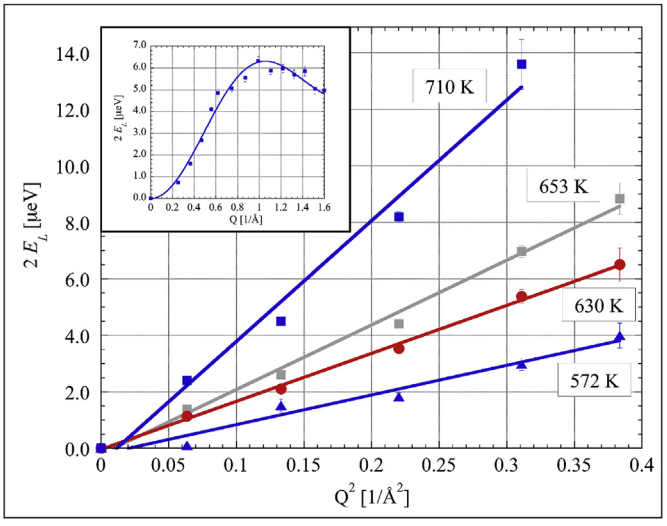

Fig. 4. Plot of Lorentzian FWHM ($2 \cdot E_L$) versus Q^2 for selected temperatures (T↑ in all cases) showing quality of fit to the low-Q expansion given by Equation (4). The fitting Q range extends to Q = 0.619 Å^{-1} (group 5) except for 710 K (Q = 0.558 Å^{-1}). The inset shows a fit of the 613 K (T↑) measurement to the general form for isotropic diffusion given by Equation (4). The first maxima of the sin $(Ql)/Ql$ term appears to be resolved. However, the best fit yields an unphysical jump distance of $l = 4.3$ Å. The sample temperatures listed correspond to the can-top TC measurement. See text for discussion.

well fit, the jump distance obtain ($l = 4.3$ Å) does not match interstitial T-T jumps of hydrogen in hexagonal Zr ($l = 1.29$ Å) and is therefore unphysical. As stated above, the Q range of the HFBS does not extend to sufficiently large values to capture the short jump distance expected for our system. It is for this reason we rely on the low-Q expansion formula, which does not depend on the jump distance. Fig. 4-inset is the best example of a maxima we observed; we therefore consider it to be unrepresentative of our QENS data in general and show it for completeness.

The measured diffusivities used to create an Arrhenius plot in Fig. 5a. We compare our diffusivity to that of Kearns [8] and others [43,44]. All diffusivities are listed in Table 3 and compared in Fig. 5b. Kearns measured diffusivity using diffusion couples fabricated from rolled plate or swaged rods of Zy-2, Zy-4, and two forms of pure Zr. Different heat treatments were also investigated by Kearns, as was the effect of sample orientation. We present three diffusivities from Kearns in Fig. 5a: an average of all data (Kearns all; Zy2, Zy4, pure Zr, heat treatment, sample orientation, and cold work), the normal direction of Zy-4, and the transverse direction of Zy-4. These diffusivities correspond to the last three entries of Table 3 from Reference 8. We resolve two trends in our diffusivity, above and below 670 K. The activation energy ($E_a = 0.461$ eV) we observed below 670 K agrees with that of Kearns ($E_a = 0.462$ eV, see Table 3).

One the other hand, the high-temperature activation energy observed here ($E_a = 0.36$ eV) is significantly (20%) lower than that of Kearns. Interestingly, our activation energy above 670 K is in better agreement with that measured by Sawatzky [43] between 533 K and 833 K (see Table 3). Kearns discussed the apparent disagreement with Sawatzky, but did not offer a conclusive explanation except to possibly implicate different experimental methods. We reserve further discussion on this topic for the next section.

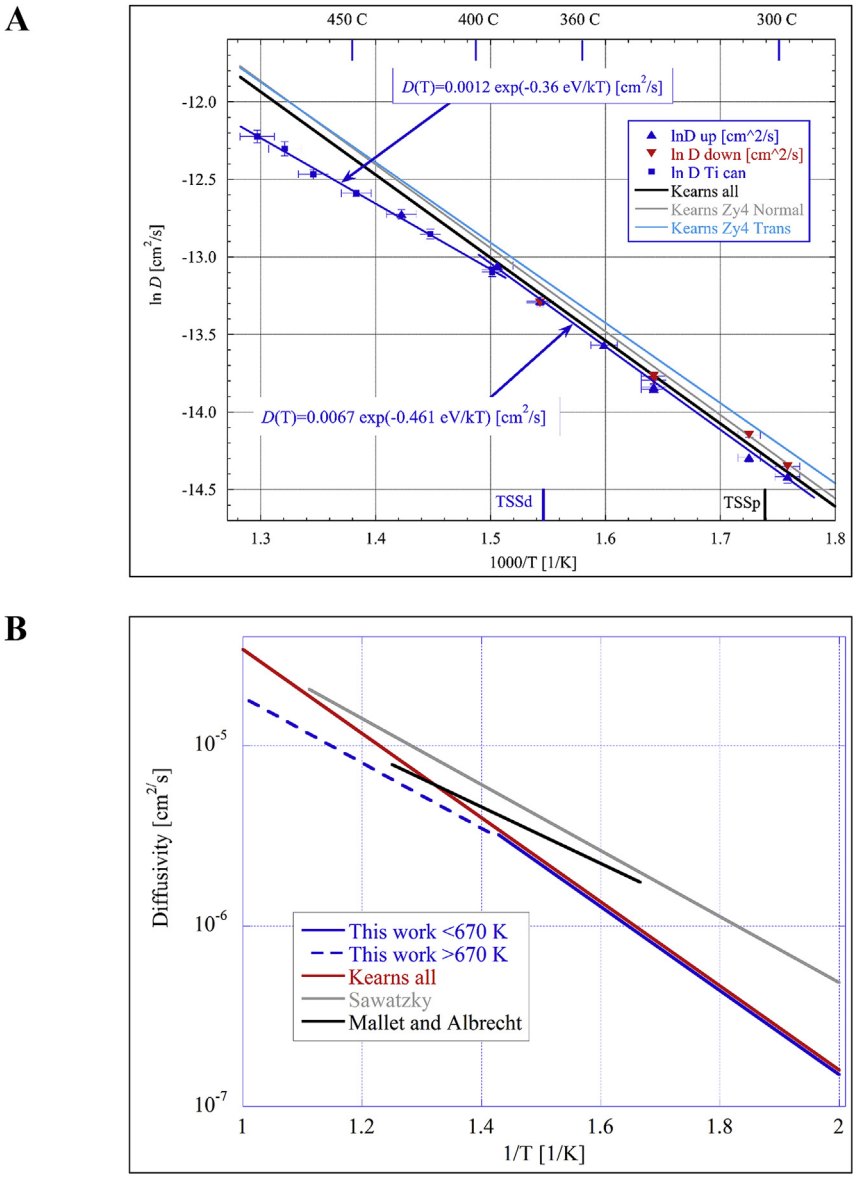

Fig. 5. a)Arrhenius plot of hydrogen diffusivity versus inverse temperature for Zy2 with 170 μg/g hydrogen concentration from this work compared to the results from Kearns [8]. We resolve two trends below and above 670 K. The activation energy for diffusion below 670 K agrees with the result of Kearns. Activation energies and diffusion constants for our work and that of Kearns are tabulated in Table 3. The x-axis error bars represent the measured temperature gradient associated with the plotted 1000/T quantity uses the average sample temperature (see text for this definition). Least-squared best fits use both x and y variable errors that are assumed to be uncorrelated [48].b)Arrhenius plot of the diffusivities measured in this work compared to the measurements of others. See Table 3 for the respective citations.

Table 3
Diffusivities from this work and the work of others.

Material	Temperature Range [K]	D_o [cm^2/s]	E_a [eV]	Reference
Zy2	572 → 670	0.0067 ± 0.0024	0.461 ± 0.019	This work
	670 → 780	0.0012 ± 0.0005	0.36 ± 0.02	
Zr, Zy2, Zy4	540 → 973	0.0070	0.462 ± 0.007	Kearns all [8]
Zy4		0.0079	0.465 ± 0.001	Kearns ND [8]
Zy4		0.0058	0.446 ± 0.005	Kearns TD [8]
Zy2	533 → 833	0.0022	0.363 ± 0.017	Sawatzky [43]
α-Zr	578 → 883	0.0007	0.31 ± 0.01	Mallett and Albrecht [44]
Zr[a]	NA	0.0011	0.434	Christensen *et al.* [9]
Zircaloy[a,b]	300 → 600	0.047	0.49	Zhang *et al.* [13]
	700 → 1100	0.0048	0.41	
δ-$ZrH_{1.58}$	~600 → 900	0.00153	0.61	Majer *et al.* [36]

[a] Advanced computational result. All others experimentally measured diffusivities.
[b] The authors of Reference [13] did not resolve two separate diffusivities above and below approximately 650 K. Instead they quote a single activation energy of 0.46 eV.

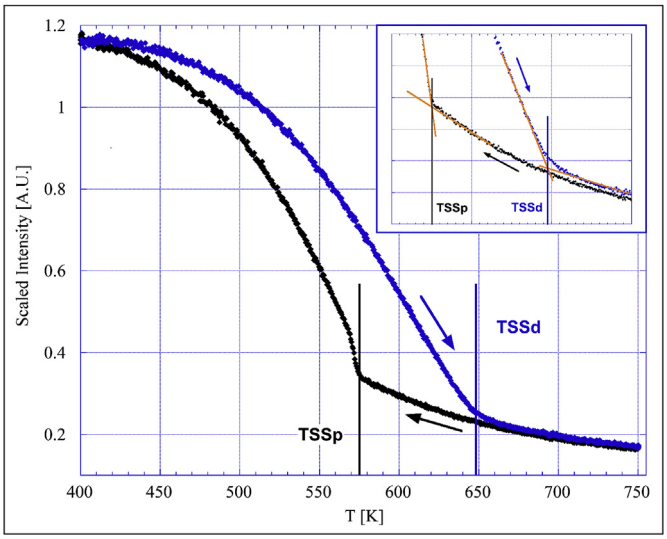

Fig. 6. Elastic intensity versus temperature for heating (blue diamond plotting symbols) and cooling (black diamond plotting symbols) from the FWS measurement. The x-axis is the can-top temperature and does not include a temperature correction. Inset shows the TSS boundary region in greater detail with axis labels omitted for clarity. A heating/cooling hysteresis is evident in the elastic intensity. Inflection points on the heating and cooling curves mark the TSS boundaries for our sample (blue and black vertical lines). The solubility limits are determined from the intersections of linear extrapolations of the elastic intensity above and below each inflection point, as shown in the inset. This is the most straightforward method in lieu of a physical model for the elastic intensity attenuation. (For interpretation of the references to colour in this figure legend, the reader is referred to the Web version of this article.)

The onset of measureable QENS intensity must coincide with hydrogen entering the solid solution phase (α-Zr). We show the elastic intensity measured in the FWS as a function temperature upon heating and cooling in Fig. 6. Diffusive motion will shift intensity beyond the elastic window and the onset of QENS is marked by a reduction of FWS elastic intensity. The TSS boundaries are marked in Fig. 6 and coincide with inflection points in the elastic intensity.

The effect of the temperature hysteresis and a greater fraction of mobile hydrogen upon cooling is demonstrated in Fig. 7, comparisons of QENS measurements for a single detector group at two steady-state temperatures reached upon heating and cooling. Greater QENS intensity (but not greater Lorentzian width) at a given temperature is expected upon cooling since a larger fraction of mobile hydrogen exists. The fact that the width does not depend on this effect is demonstrated by the diffusivities measured at common temperature listed in Table 2.

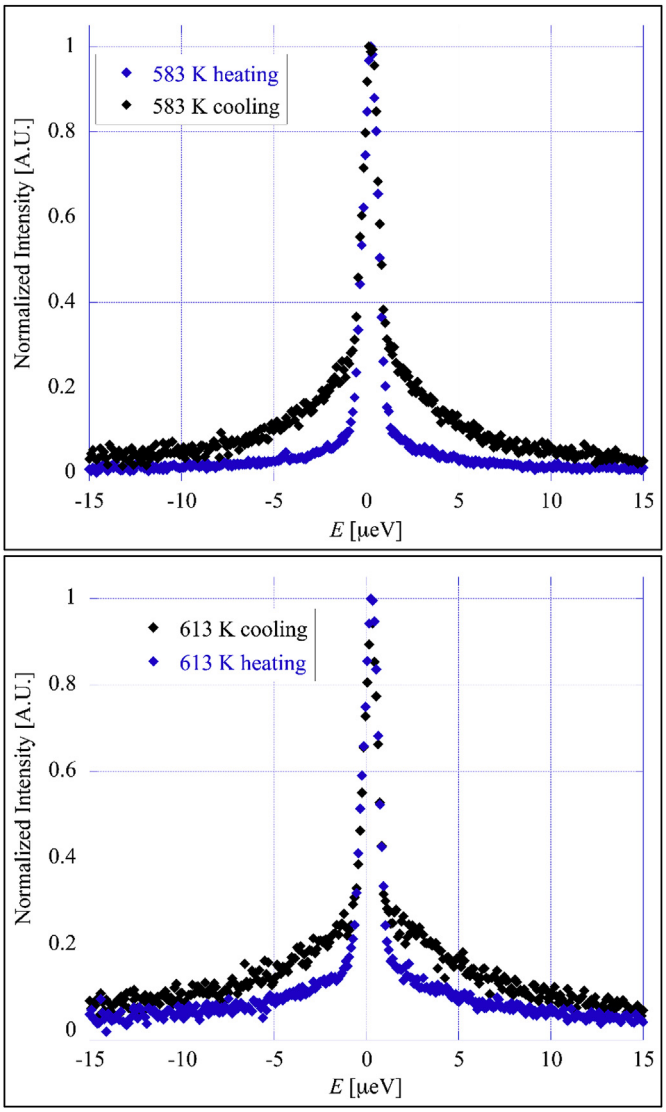

Fig. 7. Comparison of QENS measurement at (a) 583 K (top, Q = 1.217 Å^{-1}, group 10) and (b) 613 K (bottom, Q = 1.217 Å^{-1}, group 10) upon heating and cooling to reach steady-state. Larger QENS intensity upon cooling in each case, a consequence of the temperature hysteresis and a greater fraction of mobile hydrogen.

We also note the use of neutron radiography (nR) to quantify hydrogen diffusion in β-Zr [45]. This neutron-based technique has excellent sensitivity to hydrogen in metals [14] and can track

hydrogen mass transport with experimental measurement times much shorter than the QENS measurement protocols we use here. However, the nR measurements of Grosse *et al.* [45] suffer from a lack of reproducibility at common temperature points compared to our QENS results. This compromises accurate quantification of the activation energy via Arrhenius analysis.

5. Discussion

The diffusivity of hydrogen (self-diffusion) in Zy2 has been quantified using QENS. Quasi-elastic neutron scattering is directly sensitive to the diffusive motion of hydrogen solutes via line broadening analysis in the μeV energy range. This sensitivity is unique in that the technique does not rely on the existance of concentration gradients (as is the case with nR) or the use diffusion couples. We implicitly assume the self-diffusion and chemical coefficients are equivalent in our comparison of our results with the work of others. This assumption is valid in the limit of dilute solutions. Furthermore, the diffusion of hydrogen is not a binary process since the interstitial sublattice is otherwise unoccupied.

The elastic intensity in FWS measurements is attenuated by the diffusive motion of hydrogen as the solute goes into solid solution and solubility limits are marked by inflection points. This too is unique and provides clear demarcation of the TSS boundaries and is not subject to systematic error. The discussion of diffusivity and TSS limits are placed within the context of past work below.

5.1. Diffusivity of hydrogen in Zircaloy 2

The most important point of discussion is the high temperature diffusivity observed here compared to that of Kearns. Before this discussion, we point out the significant technological improvement associated with the application of QENS to study hydrogen diffusion. The work of Kearns must have taken months of sample preparation, annealing, sectioning, and hydrogen concentration analysis. Diffusivity was determined by fitting measuring hydrogen concentration gradients and the materials parameter space investigated by Kearns was extensive. However, Kearns determined diffusivity at five temperatures, two of which were close together (therefore effectively four points) and only two above 630 K. Our work required a few days of preparation of the as-received Zy2 material and approximately ten days of HFBS beam time. The measurements are directly sensitive to both hydrogen self-diffusion and solubility limits. The fact that we essentially reproduce the diffusivities of Kearns below 670 K is testament to Reference 8—this remains an important contribution to the field.

That stated, we believe our measurement represents significant correction to the diffusivity above 670 K. First, the diffusion constant is significantly lower. However D_o values determined over a narrow temperature range are strongly influenced by slight changes in E_a and we place greater emphasis on the activation energies in our discussion. The activation energy we determine above 670 K is approximately 20% lower than that of Kearns, indicating a lower barrier for diffusion. However, the actual diffusivities are lower than those measured by others (see Fig. 5b). We attribute the lower activation energy to hydrogen-impurity de-trapping in Section 5.3 but this does not explain lower diffusivities above 670 K compared to Kearns and others. The differences in overall diffusivities is likely due to different measurement techniques in the past work, possible differences in impurity concentration, and solute trapping at other defects such as dislocations. We note the extrapolation of our high temperature diffusivity to low temperature does lead to greater diffusivity compared to Kearns, consistent with greater diffusivity in the absence of trapping. Dislocations are significant solute traps. We started with a well annealed matrix and the dislocation density should be low. Our sample material cross the TSS lines repeatedly and hydride precipitation generates dislocation loops. We measure self-diffusion in the absence of a concentration gradient and these dislocations could affect the measured activation energy, either decreasing E_a (dislocation pipe diffusion [28]) if the dislocation density is high and the fraction of trapped solute is large or otherwise increasing E_a via solute trapping. Dislocation pipe diffusion reduces E_a at lower temperature [28], not at higher temperature as we observe. However, the effect of solute trapping at dislocations with a low density leading to a greater E_a at lower temperature cannot be ruled out.

Our measurements *do not* represent a convolution of fast solid solution diffusion and slower hydrogen diffusion in the δ-hydride phase since the latter process is too slow to lead to QENS beyond the elastic resolution line. Our 295-K reslution measurement demonstrates QENS is not sensitive to hydrogen diffusion in δ-hydride. If this were not the case, then a reduction in activation energy would be expected for temperatures greater than the TSSd boundary at 170 μg/g hydrogen. We could invert this argument and use our data to implicate the hydrogen diffusivity in δ-hydride from Reference 36, which is included in Table 3. However, the work of Majer *et al.*, which used pulsed-field-gradient nuclear magnetic resonance, is convincing and we reject the possibility it is not valid.

We can estimate the broadening from hydrogen diffusion in the δ-hydride phase using the diffusivity of Majer *et al.*; $E_L = 0.15$ μeV at 710 K at $Q^2 = 0.31$ Å^{-2}. This width is at the lower limit (approximately 10^{-1} μeV) of detectable line broadening for the HFBS. The Lorentzian width corresponding to solid solution diffusivity (710-K data at $Q^2 = 0.31$ Å^{-2} in Fig. 4) is approximately 7 μeV, 45 times broader. If we treat the δ-hydride phase diffusivity induced width as an inherent component of instrumental resolution, the broadening will add in quadrature with the known resolution (approximately 1 μeV) assuming Gaussian behavior; it is a 1% effect.

Most of the measurements performed by Kearns used Zy4. Zircaloy 2 was used to a lesser extent, but measurements of anneal material (the stated heat treatment for recrystallization was 788 °C for 1 h [8]) were performed at 608 K, 773 K, and 973 K. The lowest two temperatures fall in our range and the Kearns diffusivity at 608 K falls exactly on our Zy2 low-temperature fit line. The 773 K diffusivity is above our low-temperature line and is close to the "Kearns all" line in Fig. 5a. Kearns also measured cold worked Zy2 (80% cold swaged rods) at 608 and 773 K and recorded diffusivities nearly equal to the recrystallized material diffusivities. We therefore cannot attribute our high-temperature diffusivity to a materials or heat treatment effect. Kearns employed diffusion couples with all hydrogen in solid solution during annealing to induce diffusion. The diffusivities therefore were determined in material that was a single phase medium, as was ours above the TSSd upon heating and the TSSp upon cooling.

Our activation energy above 670 K is in better agreement with early work of Sawatzky [43] and Mallett and Albrecht [44] (see Table 3). However, these early diffusivities extend below 670 K and therefore disagree with our low-temperature diffusivity and the Kearns diffusivity. As we noted above, Kearns could not offer a conclusive explanation for the dissimilar activation energies, but mentioned different experimental procedures. Sawatzky for example determined diffusivity under the condition that a surface hydride persisted during the experiment [43]. The solution to the diffusion equation (Fick's second law) is not affect by a time-invariant boundary condition (constant hydrogen concentration at the surface); the procedure used by Sawatzky was designed to ensure this by maintaining the hydride phase at the free surface.

5.2. Sources of systematic error in diffusivity measurements

We discount are four sources of systematic error in our experimental protocol as explanations for the high-temperature diffusivity observed here. First, the low-Q expansion avoids potential systematic error associated with jump distance and we reproduce established diffusivity below 670 K using Equation (4). Systematic error in the sample temperature above 670 K could be responsible for our high-temperature diffusivity. The mock-up experiments described in the Materials and Methods section allowed us to directly measure the temperature gradient along the length of the sample can (the second source of systematic error). The observed gradients were accounted for in the construction of Fig. 5a Arrhenius plot. We employed a 30 min hold at temperature and confirmed steady state with respect to the QENS response. The diffusivity at 670 K was measured three times during three separate experimental runs separated by two years. These three measurements used both the Al and Ti cans and both dynamic ranges (see Table 2) and agree within statistical uncertainty. This establishes reproducibility both respect to diffusivity and temperature, eliminating possible sources of error associated with the Al versus Ti can (and vacuum versus He exchange gas, respectively), the dynamic range, and differences in the sample bar orientation within each can since bars were repacked (collectively, the third source of systematic error). We also note the 710 K (703 K corrected temperature) measurement using the Al can and the ±15 μeV dynamic range; this data point falls on high temperature diffusivity behavior in Fig. 5a for the Ti can. We therefore trust our corrected temperature values and that QENS was measured in a steady state condition at a known temperature.

The forth possible systematic error is multiple scattering. The macroscopic cross section for Zr is $\Sigma = 0.28\ cm^{-1}$ at a neutron wavelength of $\lambda = 6.271$ Å (the incident wavelength of the HFBS) and this is dominated by coherent scattering. The path length (Σ^{-1}) is approximately 3.6 cm, not too much larger than our sample radial dimension, and the effect of multiple scattering on QENS broadening needs to be considered. Three multiple scattering events are possible: elastic-elastic Zr-Zr scattering which will add intensity to the elastic peak but not induce broadening, elastic-inelastic scattering that will induce Lorentzian-type broadening, and inelastic-inelastic scattering that will also induce broadening, but much flatter and weaker (in other words, this will contribute to the linear background term using in data fitting). Significant elastic-inelastic multiple scattering will broaden the QENS component and diffusivity is proportional to the Lorentzian half width via Equation (4). Greater widths induced by multiple scattering will therefore lead to larger diffusivities. The fact that we observe the opposite above 670 K and reproduce the known diffusivity below 670 K allows us to reject multiple scattering as a significant source of systematic error.

5.3. Hydrogen solute-impurity trapping

We consider the possible effect of impurity trapping on the measured hydrogen activation energy. We do this with the caveat that other traps such as dislocations may influence the apparent activation barrier for diffusion. Zhang *et al.* studied the effect of impurity trapping on hydrogen diffusivity in kinetic Monte Carlo simulations [13]. The binding enthalpy associated with Fe, Cr, and Ni trapping were determined from first principles computation and are of the order of 0.1 eV. Tin does not trap hydrogen solutes. The effect of Fe, Cr, and Ni trapping on diffusivity in Reference [13] is similar to what we observe. The effect of oxygen was not investigated. At low temperature (below approximately 650 K) the activation energy is larger due to solute-impurity trapping influencing mass transport; the binding enthalpy adds to the activation barrier for diffusion. As the system temperature increases, impurities cease to be effective solute traps and the activation barrier then reflects regular diffusion. Although Zhang *et al.* do not resolve two separate trends in diffusivity, they are clearly present in Fig. 5a,b of Reference [13]. We have extracted Reference [13 [diffusivities and determine two activation energies above and below 650 K; these are included in Table 3. The effect of impurity trapping is to increase the activation energy by approximately 0.1 eV (0.41–0.49 eV from high temperature to low temperature).

We quantify impurity trapping by applying the Oriani model [46,47] for diffusivity with impurity traps D_{im},

$$D_{im} = \frac{D_l}{1 - \sum_i c_t^i + \sum_i c_t^i \, exp\left(E_t^i / kT\right)}, \tag{5}$$

where D_l is the lattice diffusivity in the absence of impurity traps [see Reference 13], $c_t^i = N_t c_t$ are total number trapping sites for the ith impurity (i = Fe, Cr, and Ni here), N_t is number of trapping sites for impurity i and includes both tetrahedral and octahedral interstitial hydrogen occupation, and c_t is the impurity atom concentration, and E_t^i are the binding enthalpies from Reference [13]. As with Reference [13], all impurity atoms are assumed to be in solid solution. The reader is direct to Reference [13] for details regarding the computational approach used to implement Equation (5). The calculated diffusivities of hydrogen in Zircaloy using Equation (5) are shown in Fig. 8 for four impurity concentration levels: zero or pure Zr, 0.5X or ½ the measured impurity concentrations listed in Table 1 for our Zy2 sample material, 1X or impurity concentrations equivalent to those measured, and 2X or double the measured impurity concentrations.

The activation barrier energies increase at lower temperature from 0.40 eV (lattice diffusivity, zero impurity concentration) to

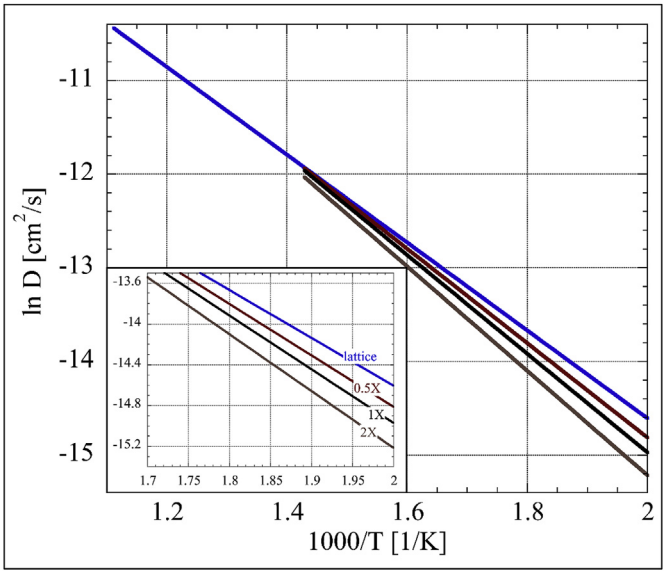

Fig. 8. Arrhenius plot of calculated hydrogen diffusivity based on the Oriani model for impurity trapping. Inset shows the low-temperature diffusivity in greater detail with axes labels omitted for clarity. The curve labeled "lattice" in the inset shows the diffusivity in the absence of impurity trap sites. The curves labeled 0.5X, 1X, and 2X represent calculated diffusivities with impurity concentration of ½, 1 times, and 2 times the measured Fe, Cr, and Ni concentration shown in Table 1. The effect of impurity trapping on diffusivity is strongest at lower temperature where the activation energy increases from 0.40 eV (lattice, no impurity trapping) to 0.48 eV (2X impurity concentration).

0.48 eV (2X impurity concentration). These activation energies are slightly lower than those determined in Reference [13] for Zircaloy due to differences in impurity concentrations. We also calculated D_{im} for 0.1X (not shown in Fig. 8). This yielded an activation energy of 0.41 eV, slightly higher than D_l in the absence of impurity trapping. The calculated diffusivities with impurity trapping merge to D_l at higher temperature with an activation energy characteristic of regular bulk lattice diffusivity. This supports our hypothesis that diffusivity we measure above 670 K is the regular bulk diffusivity for hydrogen in Zircaloy 2 in the absence of trapping.

The exact effect of impurity trapping on hydrogen solute diffusion, the cross over temperature and the change in activation energy, will depend on the solute concentration and the actual binding enthalpies. We do note that Zhang *et al.* assumed all impurities associated with the typical Zircaloy composition were in solid solution while in real cladding most metal impurities are in intermetallic second phase particles. We make the same assumption in the application of Oriani model here. This issue aside, we believe impurity trapping of hydrogen solutes provides a reasonable explanation for our observed diffusivities above and below 670 K.

Additionally, the work of Zhang *et al.* also offers a potential explanation why essentially two activation energies for hydrogen diffusion in Zr and Zr-based alloys (approximately 0.45 and approximately 0.34 eV) have been observed historically. One difficulty with this explanation is the hydrogen-impurity binding enthalpy (approximately 0.1 eV). The hydrogen solute-impurity trapping will not persist at high temperatures and regular diffusion (diffusion without trapping) should dominate. Kearns, for example, should have observed a lower activation energy at higher temperature if impurity trapping existed. . However, any effect of impurity trapping at lower temperature would be convoluted with the experimental errors associated with the methodologies employed by Kearns and others. It is also possible other unknown impurities (or other traps) with larger binding enthalpy were present in past work. The same explanation is offered by Sawatzky in discussion of pre-1960 measurements [43].

5.4. Solubility boundaries at 170 μg/g hydrogen

One advantage of the HFBS is the ability to perform fixed window scans that measure elastic intensity variation as a function of temperature. The FWS elastic intensities in Fig. 6 are affected by QENS associated with hydrogen diffusion. For example, greater quasi-elastic scattering beyond the elastic window occurs as the fraction of mobile hydrogen increases upon heating. This will cause a reduction in the elastic intensity recorded in the FWS. At the TSSd boundary all hydrogen has entered solid solution (the termination of the $\delta \rightarrow \alpha$ transformation) and further elastic intensity reduction is due to the Debye-Waller factor attenuating Zr elastic scattering. (A FWS of pure Zy2 response would be useful but was not possible because of time constraints.) The inflection point on FWS heating line is the TSSd temperature for our sample, 170 μg/g hydrogen in Zy2. This inflection occurs at $T = 647$ K, in good agreement with the TSSd boundary at 170 μg/g from Une *et al.* (655 K) [22]. Analogous reasoning holds for cooling, with an inflection point occurring when hydrogen begins to precipitate into the δ-phase. Unlike heating, however, this is the *initiation* of the $\alpha \rightarrow \delta$ phase transformation and the inflection is much sharper. This is a known behavior for phase transformations that occur during fixed window scans [35]. Further, as mentioned in Section 2.3, the temperature gradient at the TSSp was effectively zero and this would contribute to a sharper inflection. The inflection point upon cooling we observe is at $T = 575$ K; this also agrees the Une *et al.* boundary calculated at 170 μg/g (573 K [22]).

We tabulate TSS limits for pure Zr, Zy2, and Zy4 from various authors in Table 4. Large variations exist across these data, a fact that has not gone unnoticed [24]. Most solubility limits for the Zr-H system and associated alloys are obtained from differential scanning calorimetry (DSC) and this technique does not always result in well-delineated boundaries. Other methods have been applied to determine the solubility limits in Zr-H system [24], reflecting the important of the hydrogen TSS behavior in nuclear fuel cladding. As discussed by Une and Ishimoto [20], the TSSd is the more difficult boundary to determine since it represents complete dissolution. For example, the peak of the derivative of the DSC heat enthalpy output is broad (~25 °C full width half maximum) and no set convention exists for the specification of the boundary. The TSSp marks the beginning of a phase transformation and results a much sharper peak in the derivative of the DSC output. We observe similar effects related to the TSS boundaries in our FWS elastic intensities, with a broader TSSd inflection compared to the TSSp. The ~10 K temperature gradient near 650 K upon heating (Section 2.3) is a contributing factor to the broader inflection. However, the TSS limits are more clearly identifiable compared to DSC, for example, since changes in the elastic intensity are directly sensitive to the diffusive motion of hydrogen and the solute mobile fraction.

6. Summary

Our work demonstrates the utility of QENS on a backscattering spectrometer to study the Zircaloy-H system to directly measure solubility limits and diffusivity in a single experiment. The diffusivity of hydrogen in Zy2 (170 μg/g hydrogen and a formula unit of $ZrH_{0.0155}$) has been quantified as a function of temperature. QENS is sensitive the diffusive motions of atoms over the μeV energy scale and has excellent sensitivity to hydrogen in metals because of the large incoherent scattering cross section of the solute. We rely on the low-Q expansion for long-range diffusion to determine diffusivity from the Lorentzian half widths. We match the known diffusivity of Kearns [8] below 670 K. Above 670 K we find diffusion is quantified by a significantly lower activation energy (0.36 eV versus 0.462 eV). The large increase in the activation energy when the system temperature falls below 670 K is attributed to impurity trapping, although we cannot rule out trapping at dislocations. We consider impurity trapping by calculating the diffusivity using the Oriani model for Fe, Cr, and Ni impurities. At higher temperature, the impurity trapping interactions are more readily overcome (the impurity binding enthalpies are approximately 0.1 eV) and do not affect diffusivity. We therefore believe hydrogen self-diffusion in Zircaloy 2 *in the absence of trapping* is characterized by an activation energy of 0.36 eV.

The historical disparity between the Kearns diffusivity and the diffusivity measured by others has never been resolved. Our measurements appear to be a combination of the Kearns diffusivity below 670 K and the diffusivity measured by others above 670 K, an

Table 4
TSS limits for 170 μg/g hydrogen in Zr-based alloys from selected works.

Material	170 μg/g hydrogen			Reference
	TSSp [K]	TSSd [K]	ΔT [K]	
Zy2	575	647	72	This work
	573	655	82	Une *et al.* [22]
	589	663	74	Une and Ishimoto [19]
	607	658	51	Singh *et al.* [24]
Zy4	574	631	57	Vizcaino *et al.* [21]
	597	685	88	Zanellato *et al.* [20]
	601	673	72	Tang *et al.* [25]
Pure Zr	620	682	62	Une and Ishimoto [23]

observation we attribute to impurity trapping based on the work of Zhang *et al.* [13] and supported by additional Oriani model calculations. We believe impurity trapping at lower temperature is therefore a reasonable explanation for historical disparity in hydrogen diffusivity measured in Zr and Zr-based alloys such as Zircaloy. Such an effect will depend on the solid solution concentration of the metal elements found in Zircaloy and thermomechanical processing will influence metal element solubility. Oxygen impurities could be a mitigating factor as well. It is therefore impossible to state with certainty that historical measurements were not affected by impurity trapping in a non-systematic manner.

Four sources of systematic error are addressed, the jump diffusion model, sample temperature, two sample environments, and multiple scattering. We correct for the measured temperature gradient along the length of the sample in the construction of an Arrhenius plot. The effect of the jump diffusion model is eliminated via the use of the low-Q expansion. Multiple scattering is rejected based on scientific reasoning. Our experiments are insensitive to the diffusion of hydrogen in the δ-hydride phase because this diffusivity is slow and associated QENS is within the energy resolution of the instrument for all temperatures measured here.

The elastic scattering intensity versus temperature measured in fixed window scans exhibit distinct features marking the TSSd and TSSp. Elastic intensity measured in a FWS is attenuated by increasing mobile hydrogen fraction and is therefore sensitive to the hydrogen solubility limits upon heating and cooling. We match the TSS boundaries and the width of the temperature hysteresis from Une *et al.* [22] for a hydrogen concentration of 170 μg/g. Furthermore, FWS intensity analysis is straightforward to implement and is not subject to systematic error or analysis bias that may be associated with other techniques.

The hydrogen diffusivity we observe above 670 K is lower than the currently accepted diffusivity in Zr-based LWR cladding allows. For example, our diffusivity is a factor of 1.3 lower than that of Kearns at 780 K. Extrapolation of both diffusivities to 1273 K results in a factor two lower diffusivity. The time associated with diffusion scales inversely with diffusivity. Our high-temperature diffusivity would cause slower hydrogen mass transport in LWR cladding compared to the Kearns diffusivities and this could alter hydrogen release kinetics during off-normal events.

Acknowledgements

Certain commercial equipment, instruments, or materials are identified in this paper to foster understanding. Such identification does not imply recommendation or endorsement by the National Institute of Standards and Technology, nor does it imply that the materials or equipment identified are necessarily the best available for the purpose.

Access to HFBS was provided by the Center for High Resolution Neutron Scattering, a partnership between the National Institute of Standards and Technology and the National Science Foundation under Agreement No. DMR-1508249. This work was also supported by the U.S. NSF under grant number Grant No. DMR-1207102 and by the DOE NEUP ATF IRP under contract number IRP-12-4728. A portion of this work was performed at the Frederick Seitz Materials Research Laboratory Central Facilities, University of Illinois and this is gratefully acknowledged.

References

[1] O. Courty, A.T. Motta, J.D. Hales, Modeling and simulation of hydrogen behavior in Zircaloy-4 fuel cladding, J. Nucl. Mater. 452 (2014) 311–320.
[2] I. Davis, O. Courty, M. Avramova, A.T. Motta, A High-fidelity multi-physics coupling for determination of hydride distribution in Zr-4 cladding, Ann. Nucl. Energy 110 (2017) 475–485.
[3] M. Mankosa, M. Avramova, Three-dimensional multi-physics modeling of hydrogen and hydride distribution in zirconium alloy cladding, Prog. Nucl. Energy 105 (2018) 294–300.
[4] M.R. Tonks, D. Andersson, S.R. Phillpot, Y. Zhang, R. Williamson, C.R. Stanek, B.P. Uberuaga, S.L. Hayes, Mechanistic materials modeling for nuclear fuel performance, Ann. Nucl. Energy 105 (2017) 11–24.
[5] S.C. Lumley, R.W. Grimes, S.T. Murphy, P. S Burr, A. Chroneos, P.R. Chard-Tuckey, M.R. Wenman, The thermodynamics of hydride precipitation: the importance of entropy, enthalpy and disorder, Acta Mater. 79 (2014) 351–362.
[6] A.M. Jokisaari, K. Thornton, General method for incorporating CALPHAD free energies of mixing into phase field models: application to the α-zirconium/δ-hydride system, Calphad 51 (2015) 334–343.
[7] A. Aryanfar, J. Thomas, A. Van der Ven, D. Xu, M. Youssef, J. Yang, B. Yildiz, J. Marian, Integrated computational modeling of water side corrosion in zirconium metal clad under nominal LWR operating conditions, J. Met. 68 (2016) 2900–2911.
[8] J.J. Kearns, Diffusion coefficient of hydrogen in alpha zirconium, Zircaloy-2 and Zircaloy-4, J. Nucl. Mater. 43 (1972) 330–338.
[9] M. Christensen, W. Wolf, C. Freeman, E. Wimmer, R.B. Adamson, L. Hallstadius, P.E. Cantonwine, E.V. Mader, Diffusion of point defects, nucleation of dislocation loops, and effect of hydrogen in hcp-Zr: ab initio and classical simulations, J. Nucl. Mater. 460 (2015) 82–96.
[10] M. Christensen, W. Wolf, C. Freeman, E. Wimmer, R. Adamson, L. Hallstadius, P. Cantonwine, E. Mader, Effect of hydrogen on dimensional changes of zirconium and the influence of alloying elements: first-principles and classical simulations of point defects, dislocation loops, and hydrides, in: Zirconium in the Nuclear Industry: 17th, ASTM International, 2015.
[11] D. R Trinkle, Diffusivity and derivatives for interstitial solutes: activation energy, volume, and elastodiffusion tensors, Phil. Mag. 96 (2016) 2714–2735, 2016.
[12] C. Domain, R. Besson, A. Legris, Atomic-scale Ab-initio study of the Zr-H system: I. Bulk properties, Acta Mater. 50 (2002) 3513–3526.
[13] Y. Zhang, C. Jiang, X. Bai, Anisotropic hydrogen diffusion in α-Zr and Zircaloy predicted by accelerated kinetic Monte Carlo simulations, Sci. Rep. 7 (2017) 41033.
[14] J.L. Lin, W. Zhong, H.Z. Bilheux, B.J. Heuser, Azimuthally anisotropic hydride lens structures in Zircaloy 4 nuclear fuel cladding: high-resolution neutron radiography imaging and BISON finite element analysis, J. Nucl. Mater. 496 (2017) 129–139.
[15] J.L. Lin, K. An, A.D. Stoica, B.J. Heuser, Effect of external stress on deuteride (hydride) precipitation in Zircaloy-4 using in situ neutron diffraction, J. Nucl. Mater. 487 (2017) 396–405.
[16] A.T. Motta, L.Q. Chen, Hydride formation in zirconium alloys, J. Met. 64 (2012) 1403–1408.
[17] C. Lemaignan, A.T. Motta, Zirconium Alloys in Nuclear Applications, Materials Science and Technology, Wiley-VCH, New York, 1994 ch. 7.
[18] J. Bair, M.A. Zaeem, M. Tonks, A review on hydride precipitation in zirconium alloys, J. Nucl. Mater. 466 (2015) 12–20.
[19] K. Une, S. Ishimoto, Dissolution and precipitation behavior of hydrides in Zircaloy-2 and high Fe Zircaloy, J. Nucl. Mater. 322 (2003) 66–72.
[20] O. Zanellato, M. Preuss, J.Y. Buffiere, F. Ribeiro, A. Steuwer, J. Desquines, J. Andrieux, B. Krebs, Synchrotron diffraction study of dissolution and precipitation kinetics of hydrides in Zircaloy-4, J. Nucl. Mater. 420 (2012) 537–547.
[21] P. Vizcaíno, A. Flores, P. Bozzano, A. Banchik, R. Versaci, R. Ríos, Hydrogen solubility and microstructural changes in Zircaloy-4 due to neutron irradiation, in: Zirconium in the Nuclear Industry: 16th International Symposium, ASTM International, 2012.
[22] K. Une, S. Ishimoto, Y. Etoh, K. Ito, K. Ogata, T. Baba, K. Kamimura, Y. Kobayashi, The terminal solid solubility of hydrogen in irradiated Zircaloy-2 and microscopic modeling of hydride behavior, J. Nucl. Mater. 389 (2009) 127–136.
[23] K. Une, S. Ishimoto, Terminal solid solution of hydrogen in unalloyed zirconium by differential scanning calorimetry, J. Nucl. Sci. Technol. 41 (2004) 949–952.
[24] R.N. Singh, S. Mukherjee, Anuja Gupta, S. Banerjee, Terminal solid solubility of hydrogen in Zr-alloy pressure tube materials, J. Alloy. Comp. 389 (2005) 102–112.
[25] R. Tang, X. Yang, Dissolution and precipitation behaviors of hydrides in N18, Zry-4 and M5 alloys, Int. J. Hydrog. Energy 34 (2009) 7269–7274.
[26] B.J. Heuser, J.L. Lin, C. Do, L. He, Small-angle neutron scattering measurements of δ-phase deuteride (hydride) precipitates in Zircaloy 4, J. Appl. Crystallogr. 51 (2018) 768–780.
[27] B.J. Heuser, T.J. Udovic, H. Ju, Vibrational density of states measurement of hydrogen trapped at dislocations in deformed $PdH_{0.0008}$, Phys. Rev. B 78 (2008) 214101–214105.
[28] B.J. Heuser, D.R. Trinkle, N. Jalarvo, J. Serio, E.J. Schiavone, E. Mamontov, M. Tyagi, Direct measurement of hydrogen dislocation pipe diffusion in deformed polycrystalline Pd using quasielastic neutron scattering, Phys. Rev. Lett. 113 (2014) 025504–025508.
[29] B.J. Heuser, J.S. King, W.C. Chen, SANS measurements of deuteride (hydride) formation in single crystal Pd, J. Alloy. Comp. 292 (1999) 134–147.

[30] J.M. Rowe, J.J. Rush, L.A. de Graaf, G.A. Ferguson, Neutron quasi-elastic scattering study of hydrogen diffusion in a single crystal of palladium, Phys. Rev. Lett. 29 (1972) 1250–1253.
[31] J.P. Embs, F. Juranyi, R. Hempelmann, Introduction to quasielastic neutron scattering, Z. Phys. Chem. 224 (2010) 5–32.
[32] C.T. Chudley, R.J. Elliot, Neutron scattering from a liquid on a jump diffusion model, Proc. Phys. Soc. 77 (1961) 353–361.
[33] K.A. Terrani, E. Mamontov, M. Balooch, D.R. Olander, Incoherent Quasielastic Neutron Scattering study of hydrogen diffusion in thorium–zirconium hydrides, J. Nucl. Mater. 401 (2010) 91–97.
[34] M. Kofu, N. Hashimoto, H. Akiba, H. Kobayashi, H. Kitagawa, M. Tyagi, A. Faraone, J.R.D. Copley, W. Lohstroh, O. Yamamuro, Hydrogen diffusion in bulk and nanocrystalline palladium: a quasielastic neutron scattering study, Phys. Rev. B 94 (2016) 064303–064313.
[35] A. Meyer, R.M. Dimeo, P.M. Gehring, D.A. Neumann, The high-flux backscattering spectrometer at the NIST Center for Neutron Research, Rev. Sci. Instrum. 74 (2003) 2759–2777.
[36] G. Majer, W. Renz, R.G. Barnes, The mechanism of hydrogen diffusion in zirconium dihydrides, J. Phys. Condens. Matter 6 (1994) 2935–2942.
[37] ASTM International Standard B351/B351M-13, Standard Specification for Hot-Rolled and Cold-Finished Zirconium and Zirconium Alloy Bars, Rod, and Wire for Nuclear Application, 2018.
[38] G.E. Lucas, R.M.N. Pelloux, Texture and stress state dependent creep in Zircaloy-2, Metallurgical Transactions A 12 (1981) 1321–1331, 31xx.
[39] J.L. Lin, X. Han, B.J. Heuser, J.D. Almer, Study of the mechanical behavior of the hydride blister/rim structure in Zircaloy-4 using in-situ synchrotron X-ray diffraction, J. Nucl. Mater. 471 (2016) 299–307.
[40] J.I. Lin, K. An, A.D. Stoica, B.J. Heuser, Effect of external stress on deuteride (hydride) precipitation in Zircaloy-4 using in situ neutron diffraction, J. Nucl. Mater. 487 (2017) 396–405.
[41] W.C. Chen, B.J. Heuser, Solubility and kinetic properties of deuterium in single crystal Pd, J. Alloy. Comp. 312 (2000) 176–180.
[42] R.T. Azuah, L.R. Kneller, Y. Qiu, P.L.W. Tregenna-Piggott, C.M. Brown, J.R.D. Copley, R.M. Dimeo, DAVE: a comprehensive software suite for the reduction, visualization, and analysis of low energy neutron spectroscopic data, J. Res. Natl. Inst. Stan. Technol. 114 (2009) 341–358.
[43] A. Sawatzky, The diffusion and solubility of hydrogen in the alpha phase of Zircaloy-2, J. Nucl. Mater. 2 (1960) 62–68.
[44] M.W. Mallett, W.M. Albrecht, Low-pressure solubility and diffusion of hydrogen in zirconium, J. Electrochem. Soc. 104 (1957) 142–146.
[45] M. Grosse, M. Van Den Berg, C. Goulet, A. Kaestner, *In-situ* investigation of hydrogen diffusion in Zircaloy-4 by means of neutron radiography, J. Phys. Conf. Ser. 340 (2012), 012106-012113.
[46] R.A. Oriani, The diffusion and trapping of hydrogen in steel, Acta Metall. 18 (1970) 147–157.
[47] R. Kirchheim, Monte-Carlo simulations of interstitial diffusion and trapping—I. One type of traps and dislocations, Acta Metall. 35 (1987) 271–280.
[48] D. York, Least-squares fitting of a straight line, Can. J. Phys. 44 (1966) 1079–1086.